Magnetic order and magnetic properties of the oxygen deficient $SmBaMn_2O_5$ layered perovskite

J. Blasco[1], J. A. Rodríguez-Velamazán[2], G. Subías[1], M. C. Sánchez[1] and J. L. García-Muñoz[3]

[1]Instituto de Nanociencia y Materiales de Aragón, Departamento de Física de la Materia Condensada, CSIC-Universidad de Zaragoza, C/ Pedro Cerbuna 12, 50009 Zaragoza, Spain

[2] Institut Laue-Langevin, Boîte Postale 156, 38042 Grenoble, France

3 Institut de Ciència de Materials de Barcelona, ICMAB-CSIC, Campus UAB, 08193, Bellaterra, Spain

Abstract.

Magnetism in $SmBaMn_2O_5$ was investigated on a single crystal by magnetic and neutron diffraction measurements. This is an oxygen deficient perovskite with a layered ordering of Sm and Ba cations. Mn atoms are coordinated with five oxygens forming a square pyramid and they are ordered in a checkerboard pattern of expanded-compressed pyramids in the ab-plane. The neutron diffraction study revealed a ferrimagnetic ordering of Mn moments below T_N=134 K. Macroscopic measurements reveal a very anisotropic behavior. Measurements with the external magnetic field parallel ($M_{\|c}$) and perpendicular ($M_{\perp c}$) to the c-axis confirm that this is the easy axis above 10 K. Below this temperature, the Sm sublattice begins to polarize and the magnetization $M_{\|c}$ decreases while $M_{\perp c}$ experiences a huge increase. This indicates that Sm moments begin to order around 10 K in the ab-plane with a minor component on the c-axis that opposes the overall magnetization from Mn sublattices.

KEYWORDS: A. oxides; B. crystal growth; B. magnetic properties; B. magnetic structure; D. crystal structure.

1. Introduction.

Manganese oxides with a perovskite structure have been attracting considerable interest because of their magnetic and electrical properties [1,2]. The close interplay among charge, orbital and spin degrees of freedom give rise to rich phase diagrams including different types of charge, orbital and spin ordered phases [3,4]. In this way, by varying the chemical composition of the sample, materials with either giant magnetoresistance or metal-insulating transitions can be obtained [3-6]. Later on, the discovery of layered $LnBaMn_2O_{6-\delta}$ perovskites with Ln-Ba order along the c axis added a new ingredient to their complex set of interactions [7,8]. Compared to disordered or simple manganites, the layered Ln-Ba ordering strengthens ferromagnetic interactions in $LnBaMn_2O_6$ compounds with light Ln [9,10] while reinforces the charge and orbital orderings in samples with heavy Ln or Y [11-15]. In the latter compounds, the combination of layered order and the cooperative tilts of MnO_6 octahedra to relieve the enhanced structural strain (small size of Ln^{3+} versus Ba^{2+}) gives rise to multiferroic materials that present improper ferroelectricity [14-16].

$LnBaMn_2O_6$ compounds are synthesized by topotactic oxidation of $LnBaMn_2O_{6-\delta}$ ($0.5\leq\delta\leq1$) ones that are prepared by solid state reaction in reducing conditions [9,17]. The undistorted layered perovskite phase $LnBaMn_2O_6$ adopts a tetragonal *P4/mmm* structure [18] with lattice parameters $a_p\times a_p\times 2a_p$ (a_p being the cell parameter of the simple pseudocubic perovskite). It is composed of an alternating sequence of BaO_{12} and LnO_{12} cube-octahedra layers stacked along the c-axis. Mn atoms have octahedral coordination occupying a single non-equivalent site in the unit cell. In the reduced phase, $LnBaMn_2O_5$, oxygen vacancies are concentrated in the apical position of the MnO_6 octahedra but the symmetry of the aristotype phase is preserved. Accordingly, the Mn atoms have now a square-pyramidal coordination MnO_5. The Ba atom preserves the same coordination whereas the Ln atom, located on the same plane as the oxygen vacancies, is now 8-fold coordinated. Both phases contain Mn in a mixed valence state: Mn (III) / Mn (IV) in the oxidized phase and Mn (II) / Mn (III) in the reduced one. Therefore, electron localization can lead to charge ordering (CO) transitions giving rise to multiple non-equivalent sites for Mn atoms. CO transitions in $LnBaMn_2O_6$ phases have been the subject of many studies [6-15] and recently, the crystal structures of the different successive CO phases found in $SmBaMn_2O_6$ have been determined [19]. In the case of $LnBaMn_2O_5$ manganites, a CO phase has been reported in La- and Y-based compounds [9,20,21]. It is characterized by the appearance of $(h/2, k/2, l)_T$ superstructure peaks (T stands for undistorted

tetragonal cell) leading to a new tetragonal cell with lattice parameters $\sqrt{2}a_p \times \sqrt{2}a_p \times 2a_p$ and *P4/nmm* symmetry [9,21].

The topotactic oxidation/reduction processes between $LnBaMn_2O_6$ and $LnBaMn_2O_5$ phases confer a remarkable capability to intake and release oxygen to this system [22-25]. This property has attracted attention because of their potential ability for a precise control of redox reactions [26] and recent studies report that $SmBaMn_2O_{5+\delta}$ is a promising electrode material for symmetrical solid oxide fuel cells [27]. Therefore, a thorough study on the structural and physical properties of these materials is of great importance. These studies have been extensively carried out on the oxidized compounds $LnBaMn_2O_6$ but are very scarce in the reduced samples $LnBaMn_2O_5$. A study on $LaBaMn_2O_{6-\delta}$ samples reported that $LaBaMn_2O_5$ adopts a *P4/nmm* structure and undergoes a magnetic transition at 130 K. It develops a ferrimagnetic order of Mn(II) and Mn(III) moments although the experimental saturation moment was somewhat less than the theoretical one [9,21]. This type of anisotropic ferrimagnetic materials might be suitable in the construction of microwave devices like resonant isolators or circulators [28] although its low T_N (well below room temperature) suggests that fuel cell applications are more promising. The magnetic structure of G-type agreed with theoretical calculations [29] and similar results compatible with that ordering were found for $YBaMn_2O_5$ [21]. No information is yet reported about the magnetic properties of $SmBaMn_2O_5$ in spite of large amount of studies devoted to the oxidized $SmBaMn_2O_6$ compound [12,13,19]. One reason may be the difficulty of studying Sm compounds using neutron techniques due to the high neutron absorption cross section of natural Sm [30]. There are two ways to avoid this problem. The first possibility is to prepare compounds enriched in ^{154}Sm isotope. However, the cost and availability of the oxides with this isotope prevent single-crystal growth. Nevertheless, the neutron absorption strongly depends on the neutron energy [31] and high-energy neutrons (so-called hot neutrons) offer a second alternative that has successfully been used to solve magnetic structures in different Sm-based compounds [32-36].

We here report on the structural and magnetic properties of $SmBaMn_2O_5$ using a single crystal grown by floating zone and aligned along the c-axis. This has allowed us to measure the magnetic properties in the directions parallel and perpendicular to this axis, determining its great magnetic anisotropy. Moreover, the use of hot neutrons with a significant smaller absorption cross section for natural Sm permitted us to study the magnetic structure of this crystal at 12 K. Our study reveals that there are two non-

equivalent Mn sites in $SmBaMn_2O_5$. This is produced by condensation of a breathing mode of the oxygen sublattice that gives rise to a checkerboard pattern of compressed and expanded MnO_5 pyramids in the *ab*-plane. The charge segregation between the two sites is close to the expected for a couple of Mn^{2+} and Mn^{3+} cations. The magnetic structure of Mn moments is ferrimagnetic with an antiparallel coupling of Mn(II) and Mn(III) moments along the c-axis which is the easy magnetization axis. The magnetic space group has been identified as P4/nm'm'. At very low temperature, the polarization onset of Sm^{3+} moments lead to a change in the direction of the easy magnetization axis that is now perpendicular to c-axis.

2. Experimental

Single crystals of $SmBaMn_2O_5$ were grown using the floating zone method from polycrystalline precursors. Stoichiometric amounts of dried Sm_2O_3, $BaCO_3$ and Mn_2O_3 were mixed, ground and heated at 1000ºC overnight. The resulting powder was reground, pressed into pellets and sintered at 1250ºC in a gas flow of H_2/Ar mixture (2 % of H_2) saturated in water vapor to achieve a reductive atmosphere ($P_{O2} \approx 10^{-11}$). This is required to prevent the formation of $BaMnO_3$ impurity [9]. Thus, the pellets are reground, pressed into rods and sintered at 1375ºC for 24h in the same atmosphere. The rods were mounted in a homemade floating zone furnace with two semi-elliptical mirrors [37]. The growth was performed in the same reductive atmosphere with an overpressure of 2 bars. The seed and feed bars with diameters of 3.5 mm rotated in opposite directions at 20 rpm with a growth speed of 6 mm/h. Parts of the boules were cleaved to yield shiny and flat [0 0 1] faces. Other part of the boule was ground and analyzed by powder x-ray diffraction at room temperature in the range $5º \leq 2\theta \leq 135º$ using a 2θ step size of 0.03º and a counting time of 5 sec./step. Cu K_α radiation was used. The pattern was consistent with a single phase compound. The chemical composition of the powders was also tested using wavelength dispersive x-ray fluorescence spectrometry (Advant'XP+ model from Thermo-Fisher) and the Sm:Ba:Mn stoichiometry agreed with the expected values within the experimental error (1%). Oxygen content was tested by means of thermogravimetric analysis performed with a TA instruments microbalance under air flow using around 22 mg of ground crystal.

Single-crystal neutron diffraction data were collected on the high resolution four-circle diffractometer D9 at the Institute Laue Langevin (Grenoble, France) using the wavelength of 0.499(1) Å (hot source) obtained by reflection from a Cu (220)

monochromator. The wavelength was calibrated using a single crystal of Ge. A small two-dimensional (2D) area detector of 6 × 6 cm (32 × 32 pixels) allows reciprocal space survey and optimization of the peak position. The program RACER [38] was used to integrate the omega- and omega-2theta-scans and to correct them for the Lorentz factor. The crystal attenuation corrections were performed with a prism model using DATAP program, [39] with an estimated neutron absorption coefficient of 1.927 cm^{-1} [30].

Fullprof package program [40] was used for the Rietveld analysis of x-ray powder patterns and for the analysis of single-crystal neutron diffraction data. The schematic illustrations of the crystal structures were obtained with the VESTA program [41].

Magnetic measurements were carried out between 5 and 400 K by using a commercial superconducting quantum interference device (SQUID) magnetometer from Quantum Design. The measurements were performed warming the sample after zero-field cooling at an external magnetic field of 1 kOe. Isothermal magnetization measurements at selected temperatures between 5 and 250 K were performed for externals fields between -50 and 50 kOe. Both kinds of measurements were performed with the applied field parallel or perpendicular to the c-axis.

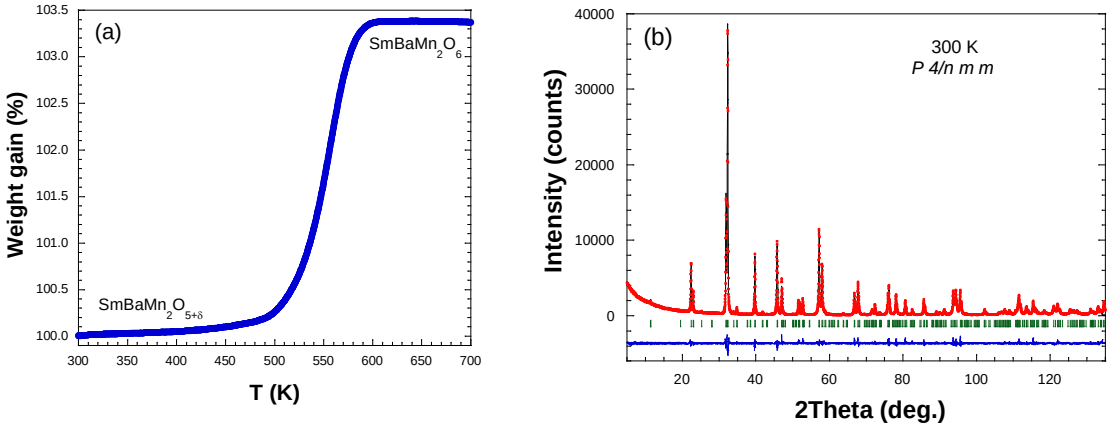

Figure 1. Weight gain versus temperature under air for $SmBaMn_2O_5$. (b) Rietveld refinement plot of the powder x-ray diffraction pattern collected at room temperature.

3. Results and discussion.

Thermogravimetric analysis (TGA) reveals that the growth conditions of our crystal give rise to a sample, $SmBaMn_2O_{5+\delta}$, with a small oxygen excess compared to the ideal formula $SmBaMn_2O_5$. Fig 1(a) displays the TGA curve unveiling that oxidation of $SmBaMn_2O_{5+\delta}$ begins at ≈500 K and finish at ≈600 K. The entire process occurs in a single step and the final product was identified as $SmBaMn_2O_6$ [19]. Assuming this phase

to be stoichiometric, the calculated value of δ is 0.11(1). This small excess of oxygen is in agreement with values reported in related compounds [9, 42]. It is also worth noting that this oxygen content is verified later in the neutron diffraction study.

Atoms	Parameters	12 K	297 K
	a (Å)	5.5449(2)	5.5966(1)
	c (Å)	7.6165(2)	7.7083(1)
	Vol. (Å^3)	234.18(1)	241.44(1)
Sm (*2b*):	B_{iso} (Å^2)	0.31(4)	0.37(4)
Ba (*2a*):	B_{iso} (Å^2)	0.14(7)	0.18(5)
Mn1 (*2c*):	z:	0.2731(12)	0.2708(7)
	B_{iso} (Å^2)	0.25(3)	0.28(3)
	μ (μ_B/at.)	3.14(3)	-
Mn2 (*2c*):	z:	0.7482(11)	0.7469(7)
	B_{iso} (Å^2)	0.25(3)	0.28(3)
	μ_z (μ_B/at.)	-4.05(4)	-
O1 (*2c*):	z	0.0062(13)	0.003(4)
	B_{iso} (Å^2)	0.33(6)	0.8(3)
O2 (*8j*):	x	0.4905(5)	0.487(2)
	z	0.3100(1)	0.3107(7)
	B_{iso} (Å^2)	0.30(5)	0.80(2)
	R_F^2	4.8	3.6
	χ^2	2.4	6.1

Table 1. Structural parameters and reliability factors from the refinements of $SmBaMn_2O_{5+\delta}$ sample at 12 K (neutron diffraction) and 297 K (x-ray diffraction). The space group is *P4/nmm*. The small oxygen excess is located at the site (¼, ¼, z≈½). The components of the Mn magnetic moments at 12 K are [0, 0, μ_z] and the magnetic space group is *P4/nm'm'*.

Fig. 1(b) shows the powder x-ray diffraction pattern and Rietveld analysis for $SmBaMn_2O_{5+\delta}$ at room temperature. The diffraction pattern could be indexed with the space group *P4/nmm* and the occurrence of the abovementioned $(h/2, k/2, l)_T$ superstructure peaks indicates that CO is present in this compound at room temperature. This also reveals that $SmBaMn_2O_5$ is isostructural to $LaBaMn_2O_5$. The refined parameters are listed in Table 1 while selected bond lengths are summarized in Table 2. The Sm, Ba, apical oxygen (O1) and basal oxygens (O2) are located at the Wyckoff positions *2b*, *2a*, *2c* and *8j*, respectively. This technique showed little sensitivity to the number of vacancies in the other apical position, so its residual oxygen occupation was set 0.1 in agreement

with the previous TGA analysis. Mn has two non-equivalent positions (denoted as Mn1 and Mn2) at *2c* sites. The Mn-O bond lengths (Table 2) disclose a checkerboard pattern of compressed and expanded MnO_5 pyramids in the *ab*-plane. Bond valence sum (BVS) calculations yields values of +2.05(6) and +3.17(6) for the Mn atoms located at the expanded (Mn2 in table 1) and compressed (Mn1 in table 1) pyramids, respectively. These values are consistent with a full Mn(II)/Mn(III) ordering between the two available sites. A schematic illustration of the crystal structure can be seen in Fig. 2. Comparing the structural data at both temperatures, the expected thermal shrinkage of the unit cell is observed. In the same way, the isotropic temperature B-factors decrease as temperature does in accordance with the reduction of atom vibrations. This decrease is more prominent in the oxygen sublattice suggesting that it is the most flexible part of the crystal structure at room temperature.

	T = 12 K	T= 297 K	Multiplicity
Sm-O2 (Å)	2.438(2)	2.461(9)	×8
Ba-O1 (Å)	2.7729(2)	2.7986(3)	×4
Ba-O2 (Å)	3.070(2)	3.109(8)	×8
Mn1-O1 (Å)	2.033(13)	2.064(31)	×1
Mn1-O2 (Å)	1.907(3)	1.901(11)	×4
Mn2-O1 (Å)	1.965(13)	1.974(31)	×1
Mn2-O2 (Å)	2.083(3)	2.129(11)	×4
Mn1-O1-Mn2 (deg.)	180	180	
Mn1-O2-Mn2 (deg.)	159.2(1)	158.6(4)	

Table 2. Selected interatomic distances and bond angles for $SmBaMn_2O_{5+\delta}$ refined from single crystal neutron diffraction (12 K) and powder x-ray diffraction (297 K).

In order to gain insights into the distortions associated to the CO phase of $SmBaMn_2O_5$, we have performed the Rietveld analysis using the symmetry-adapted modes method [43]. According to this formalism [44], the *P4/nmm* phase can be described as a superposition of distortion modes corresponding to the irreducible representations (irreps) of the undistorted tetragonal cell with symmetry *P4/mmm*. Five distortion modes corresponding to two irreps are allowed in the distortion from the *P4/mmm* phase into the *P4/nmm* one. Two modes correspond to the irrep GM1+ and are associated to the shifts of Mn and O2 atoms along the *c*-axis. These movements are also permitted in the parent *P4/mmm* phase. The other three distortions transform like irrep M2- and they are related to the k-point (½, ½, 0). A schematic representation of the atomic

shifts produced by M2- modes is included in Fig. 2. These distortions are responsible for the appearance of the (h/2, k/2, l)$_T$ superstructure peaks and the differentiation of the two Mn crystallographic sites (Mn1 and Mn2 in Fig.2). They are composed of a breathing mode of the O2 oxygens that compresses the base of a pyramid while expanding the neighboring one. A similar breathing mode is observed in the O1 atoms enlarging the height of the expanded pyramid and contracting it for the compressed one. Mn atoms move in the same direction as O1. This implies that Mn2 enters the expanded pyramid while Mn1 moves a little away from the compressed base of its pyramid. The displacement of Mn atoms is longer than that of O1. For this reason, the Mn2-O1 bond length is shorter than the Mn1-O1 one. The combination of all distortions yields the interatomic distances listed in Table 2.

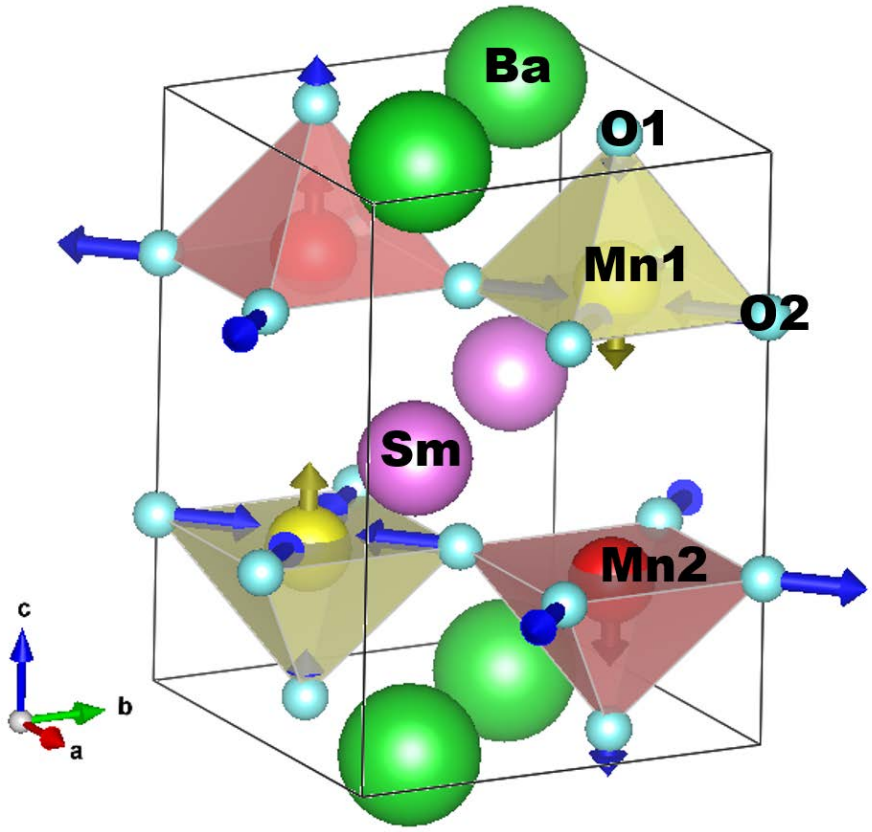

Figure 2. Crystal structure of $SmBaMn_2O_5$ at room temperature. The type of atom is indicated in the same figure and the arrows emphasize the oxygen shifts resulted from the condensation of the breathing mode and the vertical displacements of Mn atoms.

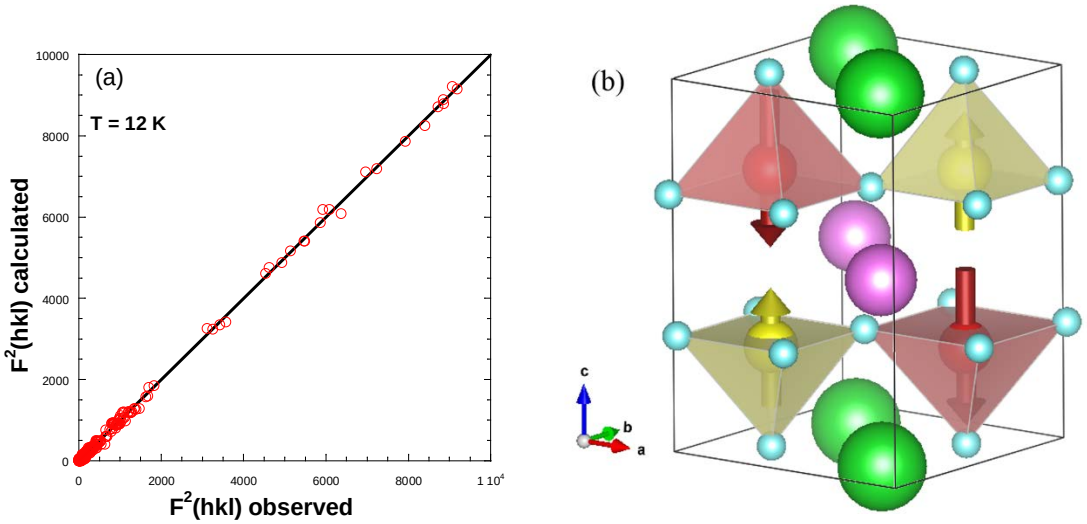

Figure 3. (a) Calculated versus observed values of the squared intensities for refined single crystal neutron diffraction data collected at 12 K for $SmBaMn_2O_5$. (b) Representation of the magnetic structure for $SmBaMn_2O_5$ at 12 K. Yellow and red colors refer to Mn1 (Mn^{3+}) and Mn2 (Mn^{2+}) sites, respectively.

The crystal and magnetic structures at 12 K were obtained from single-crystal neutron diffraction data collection of 252 reflections. The best data fit is shown in Fig. 3(a) and structural parameters are also summarized in Table 2 where comparisons with the structural data obtained at room temperature can be performed. Overall, similar structural parameters have been obtained from both techniques and the main differences in bond lengths and lattice parameters are related to the thermal contraction of the sample. The charge segregation between the two Mn sites is similar at low temperature and BVS analysis yield +3.17(2) and +2.24(2) valences for Mn1 and Mn2, respectively. This result confirms the Mn(III) / Mn(II) CO in $SmBaMn_2O_{5+\delta}$. We have verified that the space group is still *P4/nmm* so there is no structural transition from room temperature down to 12 K. The occupancy of empty apical position was also refined yielding a value of δ=0.08(2), very close to the TGA analysis. The lack of new reflections associated to the magnetic scattering confirms that the propagation vector for the magnetic structure is **k**=0. The neutron fits reveal that Mn sublattices exhibit a ferrimagnetic ordering with the moments aligned antiparallel along the c-axis. This is consistent with the magnetic space group *P4/nm'm'* (No. 129.417) or a G-type structure following the Bertaut's notation [45]. This result agrees with previous theoretical calculations that related the stability of A-type or G-type magnetic structures to the Mn1-O2-Mn2 bond angle value [29]. A bond angle less than 170º (see table 2) agrees with a greater stability of the G-type structure.

The picture of the magnetic structure can be seen in Fig. 3(b) and it is similar to related compounds [9,21]. The refined magnetic moments are 3.15(3) and 4.06(4) μ_B for Mn1 and Mn2, respectively (see Table 2). These values are smaller than the ones expected for fully polarized sublattices of Mn^{3+} and Mn^{2+} (4 and 5 μ_B, respectively) but similar to those found in $YBaMn_2O_5$ [21] and somewhat higher than those reported for $LaBaMn_2O_5$ [9]. At 12 K Sm moments keep paramagnetic. Under applied magnetic field, a saturated moment of ≈0.9 μ_B per $SmBaMn_2O_5$ formula unit (*f.u.*) is close to the theoretical one (1 μ_B / *f.u.*).

Fig. 4 shows the dc magnetization as a function of temperature for two different orientations of the single crystal: parallel (H||c) or perpendicular (H⊥c) to the c-axis. These curves disclose a strong magnetic anisotropy. A clear magnetic transition from a paramagnetic (PM) to a ferrimagnetic (FM) state is noticeable in two steps for the M(T) curve with H||c ($M_{||c}$). The first small jump with an inflection point at $T_{N'}$=181 K is followed by a big jump with an upturning point at T_N=134 K. Thus, the $M_{||c}$ value increases with decreasing temperature down to 10 K where a sudden drop is observed. Instead, in the measurement with H⊥c ($M_{\perp c}$), the first jump is hardly noticeable while a small peak is observed at 131 K that is close to the second upturning point in the $M_{||c}$(T) curve. Overall, $M_{\perp c}$ is significantly smaller than $M_{||c}$ down to ≈10 K. Below this temperature, a sharp increase in the $M_{\perp c}$(T) curve is observed (with H⊥c). This behavior is exactly the opposite of that observed in the H||c geometry and $M_{\perp c}$ overcomes $M_{||c}$ at 5 K. The macroscopic properties above 10 K are in agreement with the results obtained by neutron diffraction. The ferrimagnetic ordering of Mn moments along the c-axis agrees with an easy direction along this axis to magnetize the material. This accounts for higher magnetization values in the measurement with H||c. Regarding the two jumps observed in the M(T) curve, our opinion is that it may be related to the oxygen stoichiometry of our crystal. The oxygen excess implies that around 10% of the Mn atoms have an octahedral coordination with more Mn-O-Mn paths enhancing magnetic interactions. Therefore, oxidized zones of the crystal would order at higher temperatures while the parts with the right stoichiometry (most of the crystal) has the Néel temperature at about 134 K.

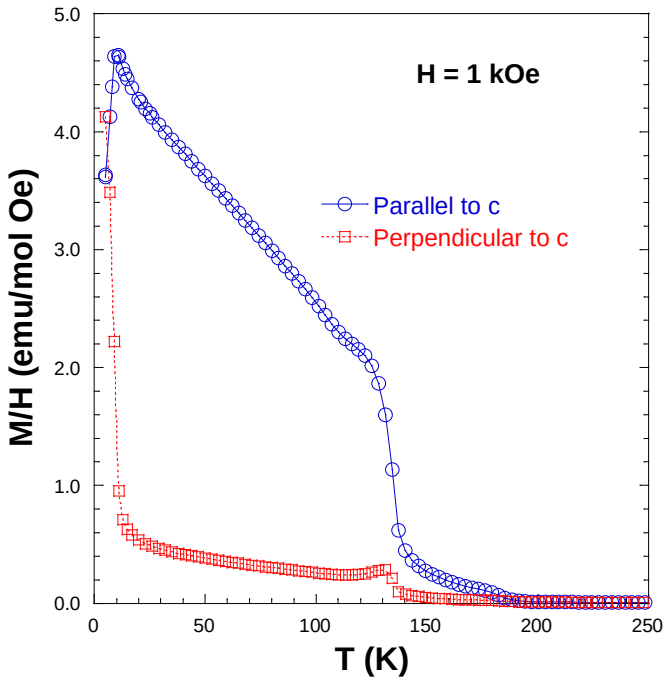

Figure 4. Magnetization vs. temperature for $SmBaMn_2O_{5+\delta}$ crystal with the magnetic field perpendicular (red squares) or parallel (blue circles) to the [0, 0, 1] direction.

The beginning of another magnetic transition is perceived in the M(T) curves below 10 K. This should be ascribed to the polarization of the Sm^{3+} sublattice that enhances the magnetism in the ab-plane while diminishes it in the c-axis. There are two possible explanations to account for these features. The first possibility is the onset of a long-range order of the Sm moments mainly located in the ab-plane with a component in the c-axis that is coupled antiparallel to the net magnetization of the Mn sublattices. Another option is a spin reorientation transition as observed in related perovskites [35,36]. In such case, the Mn moments are reoriented due to the activation of the Sm moments which are antiparallel to the uncompensated moment from Mn sublattices. In order to discern between both possibilities, hysteresis cycles have been measured at different temperatures. The measurements obtained in the two possible configurations are shown in Fig. 5.

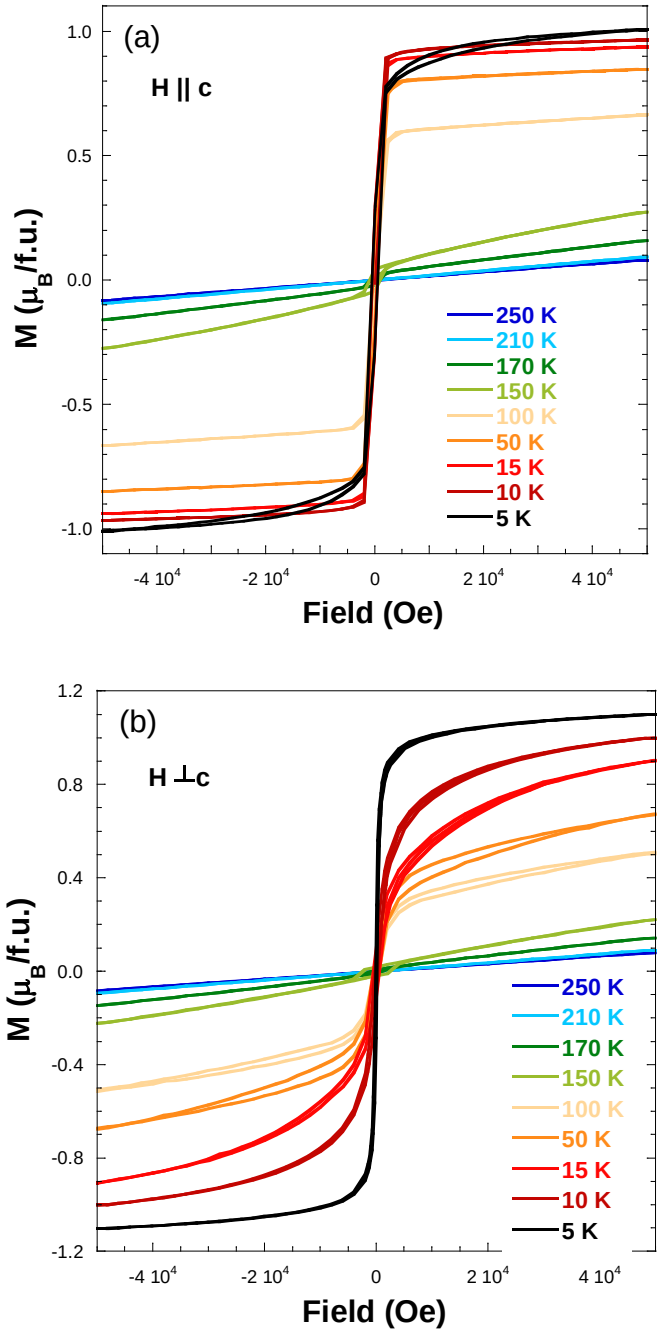

Figure 5. Isothermal magnetization curves for $SmBaMn_2O_5$ measured between 5 and 250 K with (a) H||c and (b) H⊥c.

Spontaneous magnetization is clearly noticeable in the measurements carried out at 170 K and below that temperature. Above 5 K, the measurements agree with a uniaxial magnetic anisotropy and the easy axis of the magnetization direction lies in the c-axis. Accordingly, H||c hysteresis loops are square with a very small coercive field. The direction perpendicular to this axis is harder and consequently, the loops are more oblique. Magnetic saturation is achieved in the loops at low temperature for H||c measurements.

A value close to 1 μ_B/*f.u.* at 10 K is close to the one expected for a ferrimagnetic ordering of Mn(II) and Mn(III) moments in agreement with neutron diffraction. Such a saturation is not reached in the loops measured with H⊥c even at 50 kOe. In general, magnetization is higher in the loops measured with H||c than in H⊥c for temperatures above 5 K. At this temperature, several changes are evident. The H||c loop begins to open and becomes less square while the magnetization of the H⊥c loop becomes the strongest for the first time and reaches a value of 1.1 μ_B /*f.u.* at 50 kOe. The lack of magnetic saturation in the H⊥c loop and the fact that the corresponding magnetization exceeds the expected value in the ferrimagnetic ordering of Mn sublattices points to a main contribution from Sm^{3+} moments. It is worth remembering that the ground state of Sm^{3+} ions is J=5/2 and the excited levels (J=7/2, 9/2) are not very high above the ground state so this cation is not fully polarized in the $SmBaMn_2O_5$ compound at 5 K. In any case, a partial spin reorientation of Mn moments cannot be completely ruled out due to the occurrence of Mn-Mn and Mn-Sm competitive magnetic interactions.

The raw isothermal magnetization as a function of magnetic field was simulated using the following empirical expression [46]:

$$M(H) = M_{sat} \times \tanh\left(\frac{H-H_C}{H_0}\right) + d \times H \qquad (1)$$

Where M_{sat} and H_C stand for saturation magnetization and coercive field, respectively. H_0 is a constant effective field that impedes saturation [47] while the term *d* accounts for any linear contribution to the magnetization. M_{sat} and H_C were extracted from the loops of Fig. 5 using the formula (1). The results are compared to the values of magnetization at 50 kOe in the Fig. 6. Below $T_{N'}$, spontaneous magnetization occurs and the magnetic loops exhibit a small M_{sat} but a relatively high H_C. Below T_N, the rise in M_{sat} is accompanied by a significant decrease of H_C. Therefore, the extension of the long-range magnetic order leads to a decrease in the barrier energy for magnetic domains wall. Above 5 K, the difference between the magnetization measured at the largest field (50 kOe) and M_{sat} is less in the M||H geometry than in the M⊥H one. This reflects that the sample practically reaches magnetic saturation for the M||H condition but a linear contribution is superposed for the M⊥H one. Nevertheless, this situation changes at 5 K and the magnetic saturation is closer to being reached for M⊥H. **This** change is complemented by a further decrease of H_C (Fig. 6(b)) revealing a reduction of the energy barrier for this geometry at very low temperature that may be ascribed to the onset of the magnetic arrangement in the Sm sublattice. Long range magnetic ordering of Sm^{3+} has

been already observed in simple perovskites at very low temperature [35] and it was also inferred in the $SmBaMn_2O_6$ compound [48].

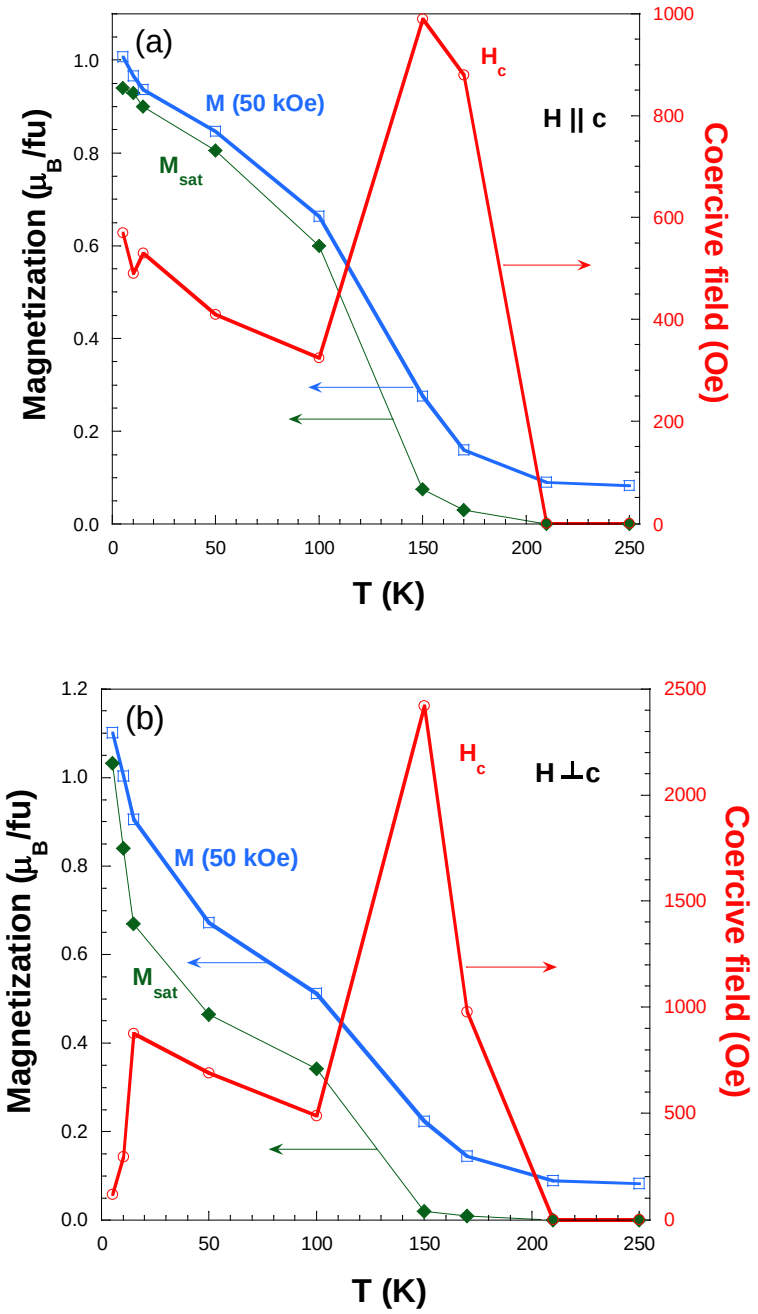

Figure 6. Temperature dependence of Magnetic saturation (M_{sat}, see Eq. (1)), magnetization at the highest field (50 kOe) and coercivity for (a) H||c and (b) H⊥c magnetic hysteresis loops of $SmBaMn_2O_{5+\delta}$.

4. Conclusions.

The structural and magnetic properties of $SmBaMn_2O_{5+\delta}$ have been studied on a single crystal specimen with a small oxygen excess ($\delta \approx 0.1$). This compound adopts a

tetragonal structure with *P4/nmm* symmetry and a checkerboard CO of Mn(II)O_5 and Mn(III)O_5 pyramids at room temperature. A symmetry analysis reveals that the main distortion associated with the stabilization of the CO is a breathing mode of the basal oxygens. The sample undergoes a ferrimagnetic transition on cooling developed in two steps. At $T_{N'}$=181 K begins the ordering of the regions with higher oxygen concentration and the hysteresis loops are characterized by a low remnant magnetization and a relatively high coercive field. Below T_N=134 K (the transition temperature corresponding to the stoichiometric pyramidal compound), the long range magnetic order extends to the entire crystal increasing the magnetic saturation and decreasing the coercivity of the magnetic loops. Single-crystal neutron diffraction reveals that magnetic moments of Mn^{2+} and Mn^{3+} sites in the CO lattice are aligned antiparallel along the c-axis that becomes the easy magnetic axis down to 10 K. At 5 K emerges the polarization of Sm^{3+} moments that lie on the ab-plane with a component along the c-axis which opposes to the net magnetization from Mn sublattices. Accordingly, magnetization in the ab-plane increases and overcomes the values of the measurements performed with the magnetic field parallel to the c-axis.

Aknowledgements. Authors would like to acknowledge the use of Servicio General de Apoyo a la Investigación from Universidad de Zaragoza. Granted beam time at ILL, is appreciated (Experiment No. 5-41-1121). For financial support, we thank the Spanish Ministerio de Ciencia, Innovación y Universidades (Projects No. RTI2018-098537-B-C22 cofunded by ERDF from EU) and Diputación General de Aragón (Project E12-20R).

References.

[1] J. M. D. Coey, M. Viret and S. Von Molnar, Adv. Phys. **48** (1999) 167-293. https://doi.org/10.1080/000187399243455.

[2] G. Subías, J. García, J. Blasco, M. G. Proietti, Phys. Rev. B **57** (1998) 748-754. https://doi.org/10.1103/PhysRevB.57.748.

[3] P. Schiffer, A. P. Ramirez, W. Bao, and S-W. Cheong, Phys. Rev. Lett. **75** (1995) 3336-3339. https://doi.org/10.1103/PhysRevLett.75.3336.

[4] J. W. Lynn, D. N. Argyriou, Y. Ren, Y. Chen, Y. M. Mukovskii, and D. A. Shulyatev Phys. Rev. B **76** (2007) 014437. https://doi.org/10.1103/PhysRevB.76.014437

[5] V. Gayathri, T. G. Kumary, E. P. Amaladass, A. T. Sathyanarayana, A. Mani, J. Superc, & novel Magn. **34** (2021) 1955–1960. https://doi.org/10.1007/s10948-021-05889-9.

[6] S. Yamada, N. Abe, H. Sagayama, K. Ogawa, T. Yamagami, and T. Arima, Phys. Rev. Lett. **123** (2019) 126602. https://doi.org/10.1103/PhysRevLett.123.126602.

[7] Y. Ueda and T. Nakajima, Prog. Solid State Chem. **35** (2007) 397-406. https://doi.org/10.1016/j.progsolidstchem.2007.01.025.

[8] D. Akahoshi, M. Uchida, Y. Tomioka, T. Arima, Y. Matsui, and Y. Tokura, Phys. Rev. Lett. **90** (2003) 177203. https://doi.org/10.1103/PhysRevLett.90.177203.

[9] F. Millange, V. Caignaert, B. Domengès, B. Raveau, and E. Suard, Chem. Mater. **10** (1998) 1974-1983. https://doi.org/10.1021/cm980130v.

[10] J. Blasco, G. Subías, M. L. Sanjuán, J. L. García-Muñoz, F. Fauth, and J. García, Phys. Rev. B **103** (2021) 064105. https://doi.org/10.1103/PhysRevB.103.064105

[11] A. J. Williams and J. P. Attfield, Phys. Rev. B **72** (2005) 024436. https://doi.org/10.1103/PhysRevB.72.024436.

[12] M. García-Fernández, U. Staub, Y. Bodenthin, S. M. Lawrence, A. M. Mulders, C. E. Buckley, S. Weyeneth, E. Pomjakushina, and K. Conder, Phys. Rev. B **77** (2008) 060402(R). https://doi.org/10.1103/PhysRevB.77.060402.

[13] E. A. Nowadnick, J. He, and C. J. Fennie, Phys. Rev. B **100** (2019) 195129. https://doi.org/10.1103/PhysRevB.100.195129.

[14] H. Sagayama, S. Toyoda, K. Sugimoto, Y. Maeda, S. Yamada, and T. Arima, Phys. Rev. B **90** (2014) 241113(R). https://doi.org/10.1103/PhysRevB.90.241113.

[15] J. Blasco, G. Subías, J. L. García-Muñoz, F. Fauth, and J. García, J. Phys. Chem. C **125** (2021) 19467-19480. https://doi.org/10.1021/acs.jpcc.1c04697.

[16] N. A. Benedek, J. M. Rondinelli, H. Djana, P. Ghosez, and P. Lightfoot, Dalton Trans. **44** (2015) 10543-10558. https://doi.org/10.1039/c5dt00010f.

[17] T. Nakajima, H. Yoshizawa, and Y. Ueda, J. Phys. Soc. Jpn. **73** (2004) 2283-2291. https://doi.org/10.1143/JPSJ.73.2283.

[18] S. V. Trukhanov, V. A. Khomchenko, L. S. Lobanovski, M. V. Bushinsky, D. V. Karpinsky, V. V. Fedotova, I. O. Troyanchuk, A. V. Trukhanov, S. G. Stepin, R. Szymczak, C. E. Botez, and A. Adair, J. Exp. and Theor. Phys. **103** (2006) 398-410. https://doi.org/10.1134/S1063776106090093.

[19] J. Blasco, G. Subías, J. L. García Muñoz, F. Fauth, M. C. Sánchez, and J. García, Phys. Rev. B **103** (2021) 214110. https://doi.org/10.1103/PhysRevB.103.214110.

[20] J. P. Chapman, J. P. Attfield, M. Molgg, C. M. Friend, and T. P. Beales, Angew. Chem. Inr. Ed. Engl. **35** (1996) 2482-2484. https://doi.org/10.1002/anie.199624821.

[21] F. Millange, E. Suard, V. Caignaert, and B. Raveau, Mat. Res. Bull. **34** (1999) 1-9. https://doi.org/10.1016/S0025-5408(98)00214-1.

[22] A. C. Tomkiewicz, M. A. Tamimi, A. Huq, S. McIntosh, J. Power Sources **330** (2016) 240-245. https://doi.org/10.1016/j.jpowsour.2016.09.013.

[23] A. M. Abdalla, S. Hossain, P. M. I. Petra, C. D. Savaniu, J. T.S. Irvine, and A. K. Azad, Mat. Lett. **204** (2017) 129-132. https://doi.org/10.1016/j.matlet.2017.06.029

[24] Y. Liu, Z. Wang, J. P. M. Veder, Z. Xu, Y. Zhong, W. Zhou, M. O. Tade, S. Wang, and Z. Shao, Adv. Energy Mater. **8** (2018) 1702604. https://doi.org/10.1002/aenm.201702604.

[25] O. L. Pineda, Z. L. Moreno, P. Roussel, K. Świerczek, and G. H. Gauthier, Sol. State Ionics **288** (2016) 61-67. https://doi.org/10.1016/j.ssi.2016.01.022.

[26] T. Motohashi, T. Takahashi, M. Kimura, Y. Masubuchi, S. Kikkawa, Y. Kubota, Y. Kobayashi, H. Kageyama, M. Takata, S. Kitagawa, and R. Matsuda, J Phys. Chem C **119** (2015) 2356-2363. https://doi.org/10.1021/jp511648b.

[27] Y. Zhang, H. Zhao, Z. Du, K. Świerczek, and Y. Li, Chem. Mater. **31** (2019) 3784-3793. https://doi.org/10.1021/acs.chemmater.9b01012.

[28] T.-H. Chang, Ferrite Materials and applications, in Electromagnetic Materials, IntechOpen, 2019. https://doi.org/10.5772/intechopen.84623.

[29] H. P. Xiang, X. J. Liu, Z. J. Wu, and J. Meng, J. Phys. Chem. B, **110** (2006) 2606-2610. https://doi.org/10.1021/jp054386h.

[30] V. F. Sears, Neutron News **3** (1992) 26-37. https://doi.org/10.1080/10448639208218770.

[31] Nuclear Date Services, http://www-nds.iaea.org/ngatlas2/

[32] D. Givord, J. Laforest, J. Schweizer, and F. Tasset, J. Appl. Phys. **50** (1979) 2008-2010. https://doi.org/10.1063/1.327141.

[33] C.-Y. Kuo, Y. Drees, M. T. Fernández-Díaz, L. Zhao, L. Vasylechko,1,4 D. Sheptyakov, A. M. T. Bell, T.W. Pi, H.-J. Lin, M.-K. Wu, E. Pellegrin, S. M. Valvidares, Z.W. Li, P. Adler, A. Todorova, R. Küchler, A. Steppke, L. H. Tjeng, Z. Hu, and A. C.

Komarek, Phys. Rev. Lett. **113** (2014) 217203. https://doi.org/10.1103/PhysRevLett.113.217203.

[34] J. Pospisil,1 G. Nénert, S. Miyashita, H. Kitazawa, Y. Skourski, M. Divis, J. Prokleska, and V. Sechovský, Phys. Rev. B **87** (2013) 214405. https://doi.org/10.1103/PhysRevB.87.214405.

[35] M. Tripathi, R. J. Choudhary, D. M. Phase, T. Chatterji, and H. E. Fischer. Phys. Rev. B **96** (2017) 174421. https://doi.org/10.1103/PhysRevB.96.174421.

[36] T. Sau, P. Yadav, S. Sharma, R. Raghunathan, P. Manuel, V. Petricek, U. P. Deshpande, and N. P. Lalla, Phys. Rev. B **103** (2021) 144418. https://doi.org/10.1103/PhysRevB.103.144418.

[37] J. Blasco, M. C. Sánchez, J. García, J. Stankiewicz, and J. Herrero-Martín, J. Cryst. Growth **310** (2008) 3247-3250. https://doi.org/10.1016/j.jcrysgro.2008.03.021

[38] M. S. Lehmann, and F. K. Larsen, Acta Cryst. A **30** (1974) 580-584. https://doi.org/10.1107/S0567739474001379.

[39] P. Coppens, Crystallographic Computing, in: F. R. Ahmed (Ed.), Munksgaard International Booksellers and Publishers Ltd., Copenhagen, 1979, pp. 255.

[40] J. Rodríguez-Carvajal, Physica B **192** (1992) 55-69. https://doi.org/10.1016/0921-4526(93)90108-I. Available at the site https://www.ill.eu/sites/fullprof/

[41] K. Momma and F. Izumi, J. Appl. Cryst. **44** (2011) 1272-1276. https://doi.org/10.1107/S0021889811038970.

[42] T. Nakajima, H. Kageyama, M. Ichihara, K. Ohoyama, H. Yoshizawa, and Y. Ueda, J. Sol. State Chem. **177** (2004) 987-999. https://doi.org/10.1016/j.jssc.2003.10.003.

[43] B. J. Campbell, H. T. Stokes, D. E. Tanner, and D. M. Hatch, J. Appl. Crystallogr. **39** (2006) 607-614. https://doi.org/10.1107/S0021889806014075.

[44] J. M. Pérez-Mato, D. Orobengoa and M. I. Aroyo, Acta Cryst. A **66** (2010) 558-590. https://doi.org/10.1107/S0108767310016247

[45] E. F. Bertaut, Acta Crystallogr. Sect. A **24** (1968) 217-231. https://doi.org/10.1107/S0567739468000306.

[46] M. J. Pitcher, P. Mandal, M. S. Dyer, J. Alaria, P. Borisov, H. Niu, J. B. Claridge, and M. J. Rosseinsky, Science **347** (2015) 420-424. https://doi.org/10.1126/science.1262118. See supplementary information.

[47] J. M. D. Coey, J. T. Mlack, M. Venkatesan, and P. Stamenov, IEEE Trans. Magn. **46** (2010) 2501-2503. https://doi.org/10.1109/TMAG.2010.2041910.

[48] R. Kiyanagi, S. Yamada, H. Aoki, H. Sagayama, T. Moyoshi, A. Nakao and T. Arima, arXiv:2107.04179v2